ARTICLE

Perovskite $CoSn(OH)_6$ nanocubes with tuned d-band states towards enhanced oxygen evolution reactions

Received 00th January 20xx,
Accepted 00th January 20xx

DOI: 10.1039/x0xx00000x

Mingwei Sun,[a, b] Baopeng Yang,[c] Jiaxing Yan,[b] Yulong Zhou,[b] Zhencong Huang,[b] Ning Zhang,*[, b] Rong Mo,*[, a] and Renzhi Ma *[, d]

The $CoSn(OH)_6$ perovskite hydroxide is a structure stable and inexpensive electrocatalyst for oxygen evolution reactions (OER). However, the OER activity for $CoSn(OH)_6$ is still unfavorable due to its limited active sites. In this work, an Fe^{3+} doping strategy is used to optimize the d-band state of $CoSn(OH)_6$ perovskite hydroxide. The $CoSn(OH)_6$ with slightly Fe^{3+} doped nanocubes is synthesized by a facile hydrothermal method. Structure characterizations show that Fe^{3+} ions were incorporated into crystal structure of $CoSn(OH)_6$. Owing to the regulation of the electronic structure, $CoSn(OH)_6$-Fe1.8% exhibits an OER overpotential of 289 mV at current density of 10 mA cm^{-2} in OER electrochemical tests. In-situ Raman spectroscopy shows that there is no obvious re-construction occurred during the OER for both $CoSn(OH)_6$ and $CoSn(OH)_6$-Fe1.8%. DFT calculations show that the introduction of Fe^{3+} into $CoSn(OH)_6$ can shift the d-band center to a relatively upper position, thus promoting the OER intermediates adsorption ability. Further DFT calculations suggests that an appropriate incorporation of Fe^{3+} into $CoSn(OH)_6$ significantly reduces the rate-determining Gibbs free energy during the OER. This work offers valuable insights into tuning d-band center of perovskite hydroxide materials for efficient OER applications.

1. Introduction

The intensifying energy crisis, driven by excessive fossil fuel consumption, is growing more seriously.[1, 2] In response to this challenge, electrochemical water decomposition has gained widespread attention as a sustainable energy conversion technology.[3, 4] The electrocatalytic process of water decomposition to produce hydrogen is seen as a promising technique achieving green and sustainable hydrogen energy.[5, 6] The main challenge in this process lies in the high dynamic barrier of the four-electron-transfer oxygen evolution reaction (OER) at the anode.[7] Currently, precious metal-based catalysts like RuO_2 and IrO_2 are considered benchmarks for industrial OER catalysts.[5, 8] However, their limited reserves and high costs constrain their commercial application.[9-11] Therefore, the development of durable, stable, and highly active non-noble metal electrocatalysts holds great significance in addressing these challenges.[12, 13]

Non-precious transition-metal-based catalysts such as phosphates, sulfides, nitrides, and hydroxides have received much attention due to their inexpensive, abundance in earth, and unique electrochemical properties.[14-18] Among them, the transition metal hydroxides, such as layered transition metal hydroxides (e.g. $Co(OH)_2$, $Ni(OH)_2$, $Ni_xFe_{1-x}(OH)_2$ et, al.), have been wide studied as electrocatalysts for OER.[19-21] However, the layered transition metal hydroxides are easily converted into oxyhydroxides during the OER process, which possibly cause the instability and reduced activity.[22, 23] The perovskite type hydroxides, such as $CoSn(OH)_6$, $MgSn(OH)_6$, $CdSn(OH)_6$, et. al., also have attracted attention.[24] The perovskite type hydroxides are chemically stable, which usually shows relatively inert phase transformation to oxyhydroxides during OER process.[25] Furthermore, the perovskite structure and contained special metal such as Sn, Ti, Fe, and Co can bring special electronic structures, which will bring unique electrochemical behaviors.[26] As a typical perovskite hydroxide, the $CoSn(OH)_6$ have electrochemical activity and stable chemical structure, which is widely studied as electrocatalysts for OER. For example, Chen et al., reported that the $CoSn(OH)_6$ perovskite hydroxide with Sn vacancies shows improved adsorption and electron transfer during the electrocatalytic OER process.[27] Wang et al reported the single-crystal $CoSn(OH)_6$ nanoboxes with a porous shell for improved OER properties.[28] Liu and co-workers demonstrated that $CoSn(OH)_6$ can be transformed into amorphous $CoSnO_x$ materials, which have promoted the OER process.[24] Although these processes have achieved for perovskite structure materials, the OER activity of perovskite $CoSn(OH)_6$ materials are still too low to be applied as practical water splitting.[29]

[a] Hunan Key Laboratory for Micro-Nano Energy Materials and Devices, School of Physics and Optoelectronics, Xiangtan University, Hunan 411105, P. R. China.
[b] School of Materials Science and Engineering, Central South University, Changsha 410083, China.
[c] School of Physics and Electronics, Central South University, Changsha 410083, China.
[d] Research Center for Materials Nanoarchitectonics (MANA), National Institute for Materials Science (NIMS), 1-1 Namiki, Tsukuba, Ibaraki 305-0044, Japan.
* Corresponding authors: Ning Zhang (nzhang@csu.edu.cn); Rong Mo (morong@xtu.edu.cn); Renzhi Ma (ma.renzhi@nims.go.jp).
Electronic Supplementary Information (ESI) available: [details of any supplementary information available should be included here]. See DOI: 10.1039/x0xx00000x

Modulating electronic d-band center over catalysts has been realized as one of the most effective strategies to optimize the energy of the binding intermediates.[30-34] Precisely controlling the location, width, and electron count of the d-band center enables adjustment of intermediate adsorption strength and reactivity, thereby optimizing the performance of OER catalysts.[35, 36] For instance, the NiO with proper exogenous doped Li^+,[37] $Ni_3Ge_2O_5(OH)_4$ with doped Fe^{3+},[38] Ni-Fe layered double hydroxides (LDH) with doped Ce^{3+} are developed to optimize the d-band states for efficient OER applications.[39] Unfortunately, tuning d-band center for perovskite based electrocatalytic materials is still seldom reported yet.

In this work, the $CoSn(OH)_6$ nanocubes with d-band center is tuned for promoting OER behaviors. The $CoSn(OH)_6$ nanocubes with different amount of Fe^{3+} doping were synthesized by a simple hydrothermal process. X-Ray diffraction (XRD) spectrum, scanning electron microscope (SEM), transmission electron microscopy (TEM), energy dispersive X-Ray spectroscopy (EDX), X-Ray photoelectron spectroscopy (XPS) prove that the $CoSn(OH)_6$ multiplies formed of nanocubes with proper Fe^{3+} doped. During the electrocatalytic measurements, $CoSn(OH)_6$ with doped 1.8 wt.% Fe^{3+} exhibited the optimized OER activity to deliver 10 mA cm^{-2} at an overpotential of 289 mV. Such a performance is much superior to the corresponding pristine $CoSn(OH)_6$. To further reveal the intrinsic mechanism of OER behaviors over these materials, the electronic states of d-band are calculated by density functional theory (DFT). With the increase of doping content of Fe^{3+}, the d-band center of $CoSn(OH)_6$ are increased. Such a change has brought more easily adsorption of OER intermediates. The work reported here has given a facile and efficient strategy to promote the OER activity over perovskite transition metal-based hydroxides.

2. Experimental

2.1 Synthesis of $CoSn(OH)_6$

Nanocrystals of perovskite hydroxide $CoSn(OH)_6$ were prepared by a hydrothermal method. In a typical procedure, Na_2SnO_3 (1.0 mmol) and $CoCl_2{\cdot}6H_2O$ (1.5 mmol) were dissolved in 20 mL deionized water separately. Then, above solutions were mixed and stirred for 10 min. Afterward, the mixed solution was transferred into a sealed Teflon-lined stainless-steel autoclave and subsequently heated on electronic oven at 200 °C for 24 h. After cooling to room temperature, the products were washed several times using distilled water and ethanol. Finally, the products were dried at 60 °C for 12 h. The obtained powders were collected and ground into a fine powder.

2.2 Synthesis of Fe^{3+} doped $CoSn(OH)_6$

The $CoSn(OH)_6$ doped with Fe^{3+} were prepared by a as same process as $CoSn(OH)_6$. The difference is that the $CoCl_2{\cdot}6H_2O$ solution is instead by different amounts of mixed solution $FeCl_3{\cdot}6H_2O$ and $CoCl_2{\cdot}6H_2O$ in 15 mL of deionized water with Fe to Co ratio of 0at. %, 2at. %, 5at. %, 8at. %. The exact composition of Fe, Sn, and Co are confirmed by inductively coupled plasma-optical emission spectrometer (ICP-OES) as Table S1 shown. According to the ICP-OES measurements, the as-prepared products were written as $CoSn(OH)_6$, $CoSn(OH)_6$-Fe0.9%, $CoSn(OH)_6$-Fe1.8%, $CoSn(OH)_6$-Fe2.7% , respectively.

More experimental details are available in ESI.

3. Results and discussion

3.1 Structure characterizations

A series of perovskite hydroxides doped with different amounts of Fe^{3+} were synthesized by hydrothermal methods. The crystal composition of the prepared products was further analyzed by XRD technique. As shown in the Fig. 1a, XRD peaks of the products are finely indexed to perovskite $CoSn(OH)_6$ (JCPDS No.13-0356), suggesting that $CoSn(OH)_6$ materials have been successfully synthesized. The enlarged figure displays the high-resolution image of (200) peaks. It is shown that the (200) peak shift to smaller angle with the Fe^{3+} doping concentration increased. Such a phenomenon is caused by that the Fe^{3+} has a larger anion radius than Co^{3+} and the cell lattice volume is expanded after doping.[40]

Fig. 1b shows the scanning electron microscopy (SEM) picture of pure $CoSn(OH)_6$. It is observed that the pristine $CoSn(OH)_6$ material was cube shape with size about 60 nm. After Fe^{3+} doping, SEM images display that $CoSn(OH)_6$-Fe0.9%(Fig. 1c), $CoSn(OH)_6$-Fe1.8%(Fig. 1d), and $CoSn(OH)_6$-Fe2.7% (Fig. 1e) have overall kept the cube-like morphology.[24] With the amount of doped Fe^{3+} content increasing, the cube-like morphology become more irregular (Fig. S1). Moreover, the corresponding energy dispersive spectrometer (EDX) is used to further analyze the element percentage data on the as prepared materials. As the EDX spectrum in Fig. S2-3 exhibited, the elemental proportions of Co, Sn and Fe are extremely similar to the result of ICP-OES.

The detailed structural information was further elucidated by transmission electron microscopy (TEM). The TEM image shows that the produced $CoSn(OH)_6$ perovskite hydroxide has a cube-like shape with a size is approximate 60 nm (Fig. 1f). The $CoSn(OH)_6$ perovskite hydroxide exhibits closed perpendicular morphology with uniform contrast, as seen by the high-resolution TEM (HRTEM) image (Fig. 1g). The corresponding Fast Fourier Transform (FFT) pattern in inset of Fig. 1g reflects that the obtained $CoSn(OH)_6$ exhibits crystallinity of the products.[27] The TEM image of $CoSn(OH)_6$-Fe1.8% shows that the obtained $CoSn(OH)_6$-Fe1.8% perovskite hydroxide has the same morphology as the $CoSn(OH)_6$ (Fig. 1h). Corresponding selected area electron diffraction (SAED) shows a set of clear diffraction spots, which can be indexed to (020), (220), and (200) crystal facets of perovskite $CoSn(OH)_6$ (inset of Fig. 1h), suggesting single crystal property of the as prepared $CoSn(OH)_6$ materials.[41] Furthermore, the HR-TEM image of $CoSn(OH)_6$-Fe1.8% shows that the lattice spacing value is calculated to be 0.38 nm, matching the $CoSn(OH)_6$ lattice plane (200) (Fig. 1i).[28] According on the FFT pattern, the resulting $CoSn(OH)_6$-Fe1.8% has an octahedral structure (inset of Fig. 1i).[40] In addition, the elemental mapping image of $CoSn(OH)_6$-Fe1.8% from EDX and

the high-angle annular dark-field scanning TEM (HAADF-STEM) image in Fig. 1j show that the Co, Sn and Fe elements are homogeneously distributed in $CoSn(OH)_6$-Fe1.8% nanocubes, suggesting that the $CoSn(OH)_6$ nanocubes is evenly doped with Fe^{3+}. Above investigations confirm that we have successfully synthesized the Fe^{3+} doped $CoSn(OH)_6$ nanocubes. The proposed crystal scheme is shown in Fig. 1k, the Sn, Co, Fe, and O atoms were composed in form as cubic like perovskite structure. The doping of Fe are formed by replacing slightly amount of Co.[27]

3.2 Elemental states

The element states of as prepared $CoSn(OH)_6$ materials were further investigated by X-ray photoelectron spectroscopy (XPS). The $C1_S$ from adventitious carbon (284.8 eV) was used to calibrate the XPS spectra. Fig. 2a displays the Co 2p spectra of $CoSn(OH)_6$ and $CoSn(OH)_6$-Fe1.8%. The center of Co^{2+} and Co^{3+} states signal peak of Co 2p of $CoSn(OH)_6$ are 783.1 and 781 eV, respectively.[42] The center of Co^{2+} and Co^{3+} states signal peak of Co 2p of $CoSn(OH)_6$-Fe1.8% are 782.8 and 780.8 eV, respectively.[43] It demonstrates that $CoSn(OH)_6$-Fe1.8%'s Co 2p banding energy peaks move to a lower energy than that of $CoSn(OH)_6$, which indicating that the electron cloud round Co atom become more concentration after the incorporation of Fe.[44] Fig. 2b shows the Sn 3d XPS spectra of $CoSn(OH)_6$ and $CoSn(OH)_6$-Fe1.8%. The signal peaks of Sn $3d_{5/2}$ and Sn $3d_{3/2}$ of $CoSn(OH)_6$ are mainly concentrated at 486.6 and 495 eV. In addition, the Sn $3d_{5/2}$ and Sn $3d_{3/2}$ signal peaks of $CoSn(OH)_6$-Fe1.8% are mainly concentrated at 486.5 and 494.9 eV. Such a result shows indicates that the main characteristics of Sn^{4+}

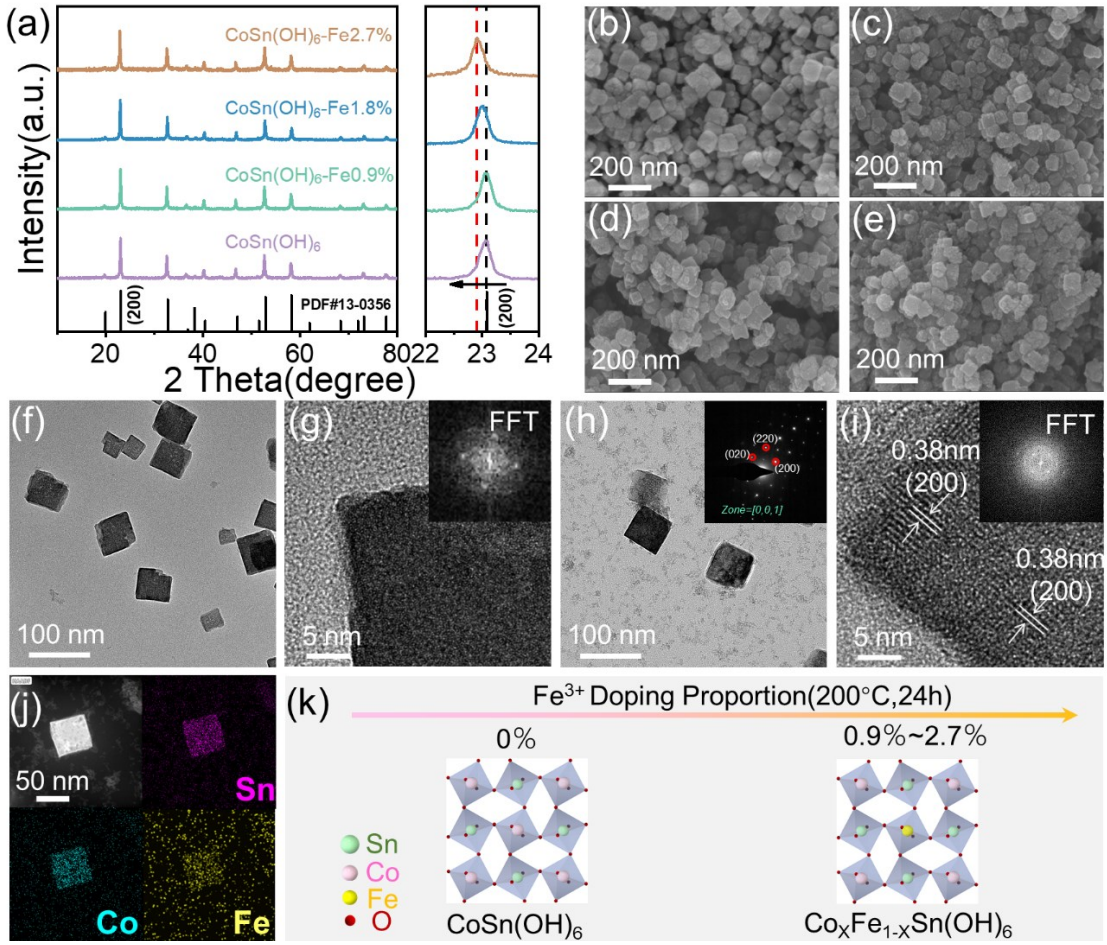

Fig. 1 (a) XRD patterns of and SEM (b-e) images of $CoSn(OH)_6$, $CoSn(OH)_6$-Fe0.9%, $CoSn(OH)_6$-Fe1.8%, and $CoSn(OH)_6$-Fe2.7%; (f) TEM image of $CoSn(OH)_6$; (g) HR-TEM image of $CoSn(OH)_6$, inset is the corresponding FFT diffractions. (h) TEM image and SAED, (i) HR-TEM image (inset is the FFT patterns), and (j) HAADF-STEM images of $CoSn(OH)_6$-Fe1.8% and the EDX elemental maps of Sn, Co, and Fe; (k) The scheme of structure evolution process of $CoSn(OH)_6$ nanocubes doped with Fe at different proportions.

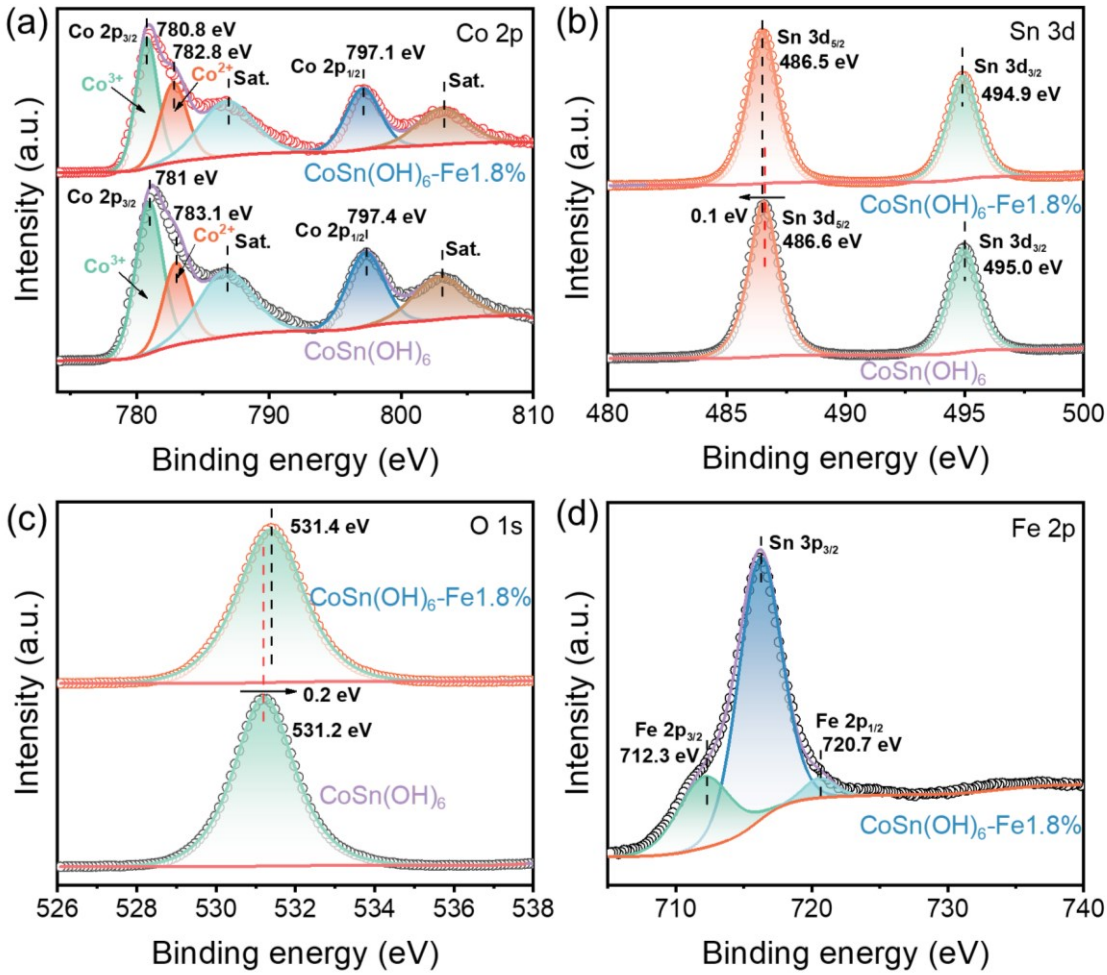

Fig. 2 XPS spectra of (a) Co 2p, (b) Sn 3d, (c) O 1s, and (d) Fe 2p.

states exist in $CoSn(OH)_6$ and $CoSn(OH)_6$-Fe1.8% samples.[45] Meanwhile, in comparison with pristine $CoSn(OH)_6$, the 3d orbital energy of Sn^{4+} in the $CoSn(OH)_6$-Fe1.8% sample was negatively shifted, indicating that the electron round Sn atom become thicker after the incorporation of Fe. As shown in Fig. 2c, the peak of fitted curves of $CoSn(OH)_6$-Fe1.8% in the O 1s XPS spectrum is positively shifted in comparison to $CoSn(OH)_6$, indicating that the electron cloud around O atom provides becomes thinner after the incorporation of Fe^{3+}.[46] The existence of the element Fe is thus confirmed by the high-resolution Fe 2p XPS spectrum over $CoSn(OH)_6$-Fe1.8% sample (Fig. 2d). Th Fe $2p_{3/2}$ and Fe $2p_{1/2}$ of Fe^{3+} are represented by the peaks at 712.3 and 720.7 eV, suggesting the existence of Fe+3 state.[47] Based on above analysis, it could be deduced that the Fe^{3+} doping efficiently modulated the electronic structure of $CoSn(OH)_6$.[48]

3.3 Electrocatalytic OER performance

At a scan rate of 10 mV s^{-1}, the catalysts' OER activity was assessed in O_2-saturated 1.0 M KOH (see details in Supporting Information). The linear sweep voltammetry (LSV) curves scanned at 10 mV s^{-1} are displayed in Fig. 3a. It can be seen that the Fe^{3+} doped $CoSn(OH)_6$ have reduced OER overpotentials than the pristine $CoSn(OH)_6$. The OER activity of Fe^{3+} doped $CoSn(OH)_6$ thus improved gradually along with the Fe^{3+} doping ratio and CoSn(OH)6-Fe1.8% achieved the relatively optimized activity. At a current density of 10 mA cm^{-2}, the overpotential of $CoSn(OH)_6$-Fe1.8% for the OER was determined to be 289 mV. The results show that the electrochemical OER performance of $CoSn(OH)_6$ is significantly influenced by the doping amount of Fe^{3+}. For comparison purpose, the CoFe-LDH ($Co_{0.982}Fe_{0.018}(OH)_x$) was also investigated (Fig. S4), the $CoSn(OH)_6$-Fe1.8% also shows relatively reduced overpotentials at 10 and 50 mA cm^{-2}, indicating the perovskite exhibit superior OER activity compared to corresponding layered hydroxides. The overpotentials at 10 and 50 mA cm^{-2} were compared (Fig. 3b). The highest overpotential of 383 mV was observed in the pristine $CoSn(OH)_6$ at the current density of 10 mA cm^{-2}. Otherwise, the OER overpotentials of 325, 289, and 293 mV at 10mA cm^{-2}, were much lower for the $CoSn(OH)_6$-Fe0.9%, $CoSn(OH)_6$-Fe1.8%, and $CoSn(OH)_6$-Fe2.7%, respectively. At the current density of 50 mA cm^{-2}, the trend remains the same, where the $CoSn(OH)_6$, $CoSn(OH)_6$-Fe0.9%, $CoSn(OH)_6$-Fe1.8%, and $CoSn(OH)_6$-Fe2.7% require overpotentials of 479, 415, 366, and 436 mV, respectively. According to these analysis, the $CoSn(OH)_6$-Fe1.8% possess an optimized electrochemical activity when compared to the pristine $CoSn(OH)_6$.[24]

The Tafel slope (Fig. 3c) was used to determine the OER kinetics of these samples. The $CoSn(OH)_6$-Fe1.8% showed the lowest Tafel slope (54.34mV dec^{-1}) in comparison with to $CoSn(OH)_6$-Fe0.9% (72.13mV dec^{-1}), $CoSn(OH)_6$-Fe2.7% (75.72mV dec^{-1}), and pristine $CoSn(OH)_6$ (87.23mV dec^{-1}), confirming the optimized synthetic condition locates at $CoSn(OH)_6$-Fe1.8% product. The electrochemical impedance spectroscopy (EIS) was obtained at 1.60 V vs RHE (Fig. 3d). Fitting the EIS spectra with an equivalent circuit yields the solution resistance (R_s) and charge transfer resistance (R_{ct}) (inset of Fig. 3d).[27] Every sample has the R_s of around 6.2 Ω (Table S2), indicating a comparable electrochemical test condition.[38] The R_{ct} was obtained by fitting the semicircle in low frequency.[39] As shown in Fig. 3e, the R_{ct} which represents the charge transfer surface intermediate resistance is ranked in the same order in alkaline electrolyte: $CoSn(OH)_6$-Fe1.8% (11.5 Ω) < $CoSn(OH)_6$-Fe0.9% (18.1 Ω) < $CoSn(OH)_6$-Fe2.7% (63.2 Ω) < $CoSn(OH)_6$ (100.8 Ω). The $CoSn(OH)_6$-Fe1.8% anode thus shows the smallest bulk charge transport resistance. The optimized R_{ct} over $CoSn(OH)_6$-Fe1.8% is beneficial to the charge and mass transfer and during the OER process. In addition, the OER performance of $CoSn(OH)_6$-Fe1.8% with already reported Fe, Co, and Sn based materials are compared. The OER activity of the as-prepared $CoSn(OH)_6$-Fe1.8% is comparatively favorable (Table S3).

The electrochemically active surface area (ECSA) calculated by double-layer capacitance (C_{dl}) are studied to reveal the intrinsic electrocatalytic activity of the Fe^{3+} doped $CoSn(OH)_6$. The CV test was conducted between 1.35 and 1.45V (vs RHE) was used to determine the C_{dl} value (Fig. S5). As illustrated in Fig. 3f, the capacitance of $CoSn(OH)_6$, $CoSn(OH)_6$-Fe0.9%, $CoSn(OH)_6$-Fe1.8%, and $CoSn(OH)_6$-Fe2.7% was determined to be 30.99, 35.61, 39.83, and 49.84 μF cm^{-2}, respectively. Then we normalized the LSV curves of Fe^{3+} doped $CoSn(OH)_6$ samples by ECSA, the Fe^{3+} doped sample still has higher intrinsic activity with the lowest overpotential locates at $CoSn(OH)_6$-Fe1.8% as shown in Fig. 3g. Therefore, the Fe^{3+} doping significantly increases the intrinsic activity of $CoSn(OH)_6$ rather than only enhances the ECSA. Further evaluation of the $CoSn(OH)_6$-Fe1.8% catalyst's durability was conducted using chronopotentiometric (CP) measurement at room temperature and a fixed current density of 10 mA cm^{-2} (Fig. 3h). The potential of $CoSn(OH)_6$-Fe1.8% rises by just 20 mV over 26 hours to maintain a current density of 10 mA cm^{-2}. Meanwhile, the durability of $CoSn(OH)_6$-Fe1.8% catalyst was further tested by chronopotentiometric test at fixed current densities of 100 mA

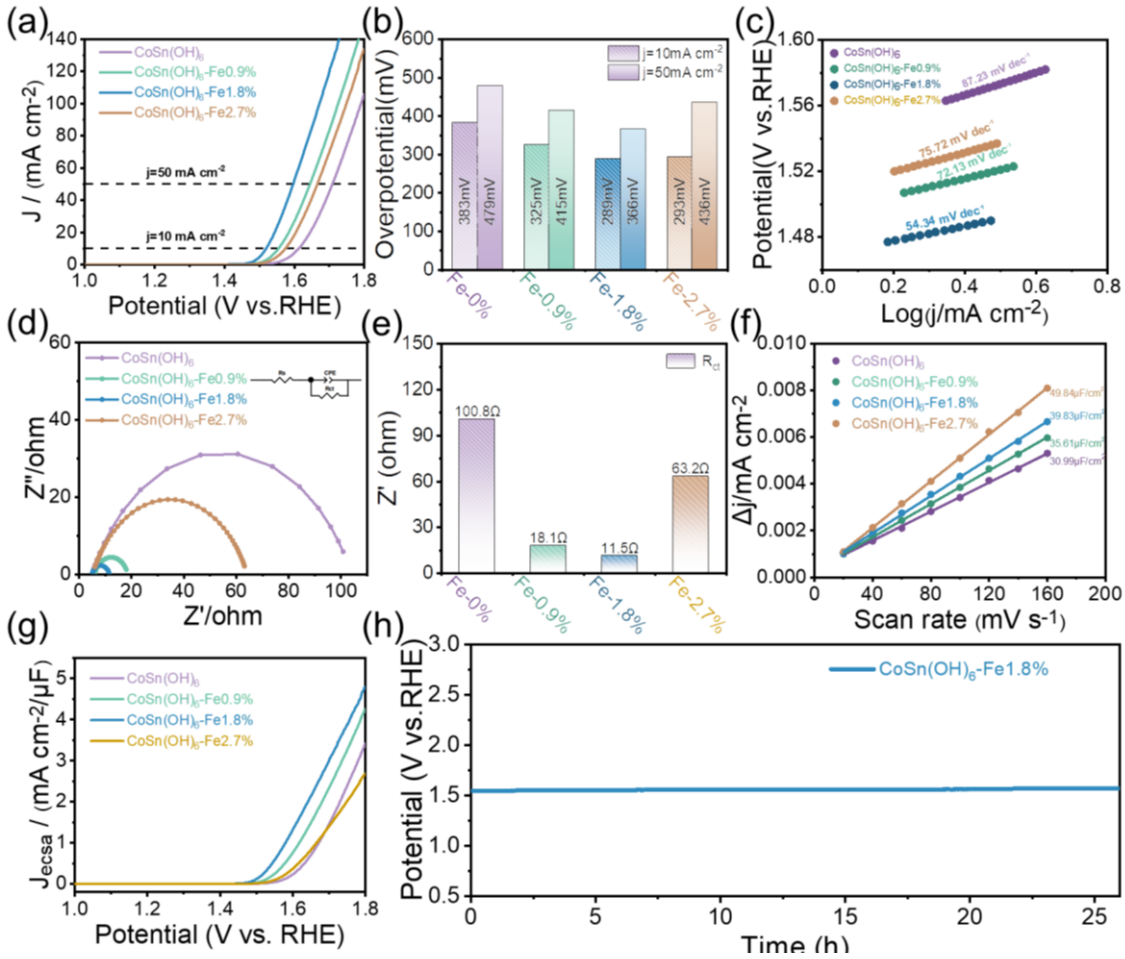

Fig. 3 (a) LSV curves; (b) Calculated overpotentials at 10 mA cm^{-2} and 50 mA cm^{-2}; (c) The LSV-derived Tafel slopes; (d) EIS analysis at 1.6 V vs RHE (the inset is the model of equivalent circuit); (e) Impedance values of different samples; (f) current density difference plotted against scan rates; (g) LSV curves normalized with ESCA. (h) Chronopotentiometry curves of $CoSn(OH)_6$-Fe1.8% at 10 mA cm^{-2}.

cm^{-2} at room temperature (Fig. S6), which also shows favorable stability. A comparison of the morphology before and after the electrochemical reactions is shown in Fig. S7. After the stability measurement, the morphology is almost kept.

3.4 In-situ electrochemical characterizations

The $CoSn(OH)_6$-Fe1.8% and pristine $CoSn(OH)_6$ were characterized using in-situ Raman spectroscopy in order to gain insights into the structural changes in electrochemical OER test (Fig. 4a). The carbon fiber paper substrate has three identical Raman bands at 416, 575, and 749 cm^{-1} (Fig. 4b-c, Fig. S8). The Co-O vibration in $CoSn(OH)_6$ could be assigned to the other Raman band at 479 cm^{-1}, as demonstrated by the in-situ Raman spectra of pristine $CoSn(OH)_6$.[49, 50] Furthermore, there was no obvious shift in the peak's position or the appearance of new bands as exhibited in the whole applied potential range. The structure of $CoSn(OH)_6$ material is stable under the OER process. The $CoSn(OH)_6$-Fe1.8% sample shows the same result, suggesting that the structural is stable during the OER test. There is an extra Raman band (601 cm^{-1}) in $CoSn(OH)_6$-Fe1.8% sample (Fig. 4c), which is attributed to the Raman band corresponding to the Fe-O vibration from the produced Fe-O(OH).[50, 51] The XRD spectra before and after OER have also examined, which also consistent with the in-situ Raman results (Fig. S9). It is reported that most layer hydroxides materials such as $Ni(OH)_2$ and $Co(OH)_2$ converted into oxyhydroxides (e.g. NiOOH and CoOOH) during the OER process.[19, 52] For $CoSn(OH)_6$ materials, such a re-construction is not obviously observed, suggesting the superior stability of perovskite structure during the electrochemical OER process.

3.5 DFT calculations

To further gain deep insight into the influence of Fe^{3+} on OER performance over $CoSn(OH)_6$. The d-band states are studied by density functional theory calculations (DFT). The corresponding atomic model of $CoSn(OH)_6$ and $Co_{0.83}Fe_{0.17}Sn(OH)_6$ are displayed in Fig. 5a-b. The (001) surface of $CoSn(OH)_6$, and $Co_{0.83}Fe_{0.17}Sn(OH)_6$ were constructed to simulate the surface of catalysts, which contained two octahedral layers (Fig. S10). Fig. 5c-d shows the partial density of states (PDOS) 3d orbits calculated on the corresponding atomic model.[24, 53] The d-band states of these catalysts are near the Fermi level.[30] The electronic structure of $CoSn(OH)_6$ perovskite hydroxide has changed after Fe^{3+} doping. The calculated d-band centers of $CoSn(OH)_6$, and $Co_{0.83}Fe_{0.17}Sn(OH)_6$ are approximate -2.21 and -1.95 eV, respectively. The value of d-band center increases after the increase of Fe^{3+} content. It is known that the filling degree of the antibonding state can be reflected from the location of the d-band center with respect to the Fermi level.[31] The higher center of the d band, the fewer electrons are filled to the antibonding state, which will result in a stronger bond between the adsorbent and the catalyst.[54] Compared to $CoSn(OH)_6$, the d-band center of $Co_{0.83}Fe_{0.17}Sn(OH)_6$ perovskite hydroxide is

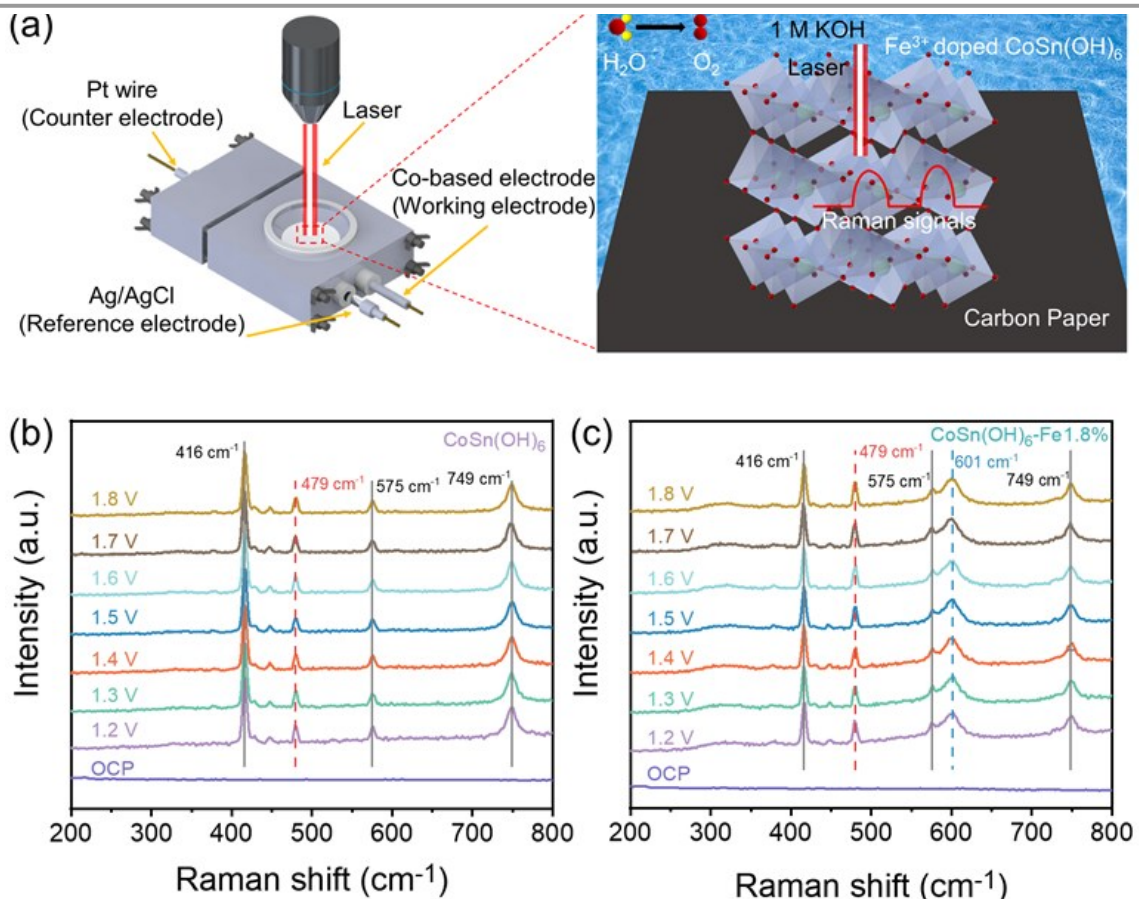

Fig. 4 (a) Schematic illustration of the in-situ Raman spectroscopy setting; In-situ Raman spectra of (b) $CoSn(OH)_6$, and (c) $CoSn(OH)_6$-Fe1.8% at different potentials.

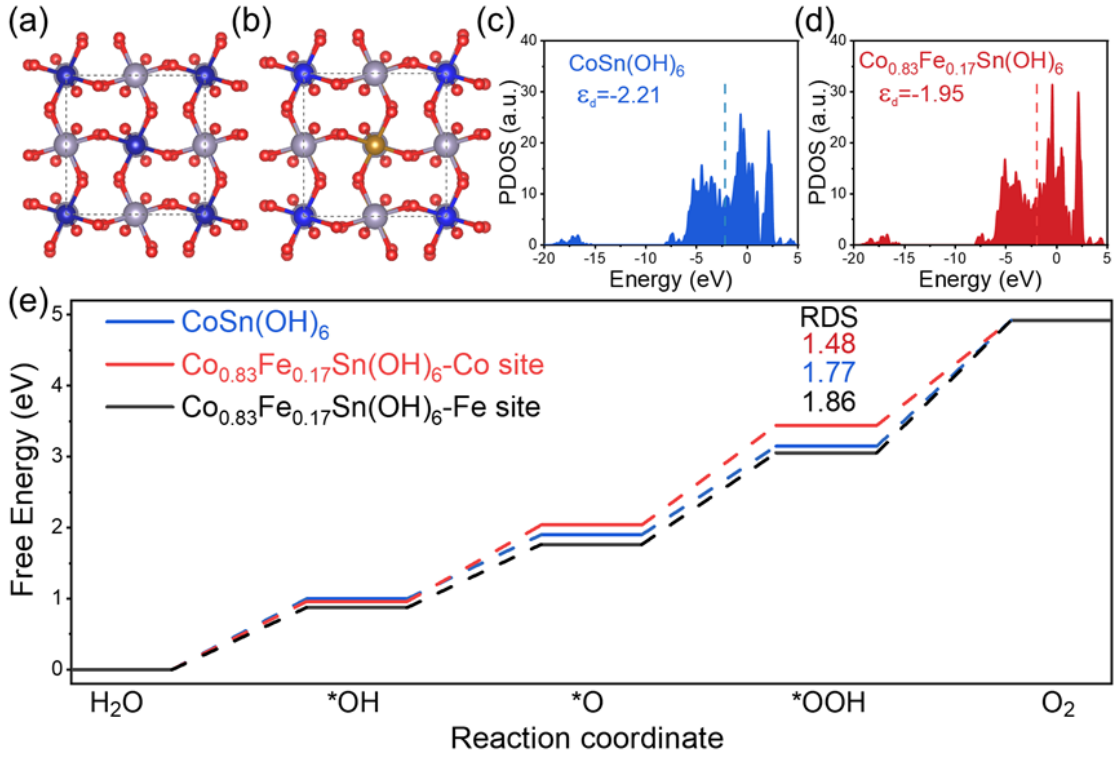

Fig. 5 Schematic changes of bond structure for (a) $CoSn(OH)_6$, and (b) $Co_{0.83}Fe_{0.17}Sn(OH)_6$; The PDOS of 3d orbits for (c) $CoSn(OH)_6$, and (d) $Co_{0.83}Fe_{0.17}Sn(OH)_6$; (e) The reaction Gibbs free energy changes during the OER process.

higher, indicating a relatively stronger adsorption ability between active sites and intermediates.

In addition, to study the influences of d-band states on the intermediates' adsorption on these materials, the reaction Gibbs free energies of *OH, *O, and *OOH intermediates adsorbed on $Co_{0.83}Fe_{0.17}Sn(OH)_6$ surface were calculated (Fig. S11-12).[55] Fig. The Gibbs free energies of *OH, *O, and *OOH at different active sites is displayed in Fig. 5e. The *O to *OOH are the rate-determining steps for the various active sites. The Co and Fe sites in $Co_{0.83}Fe_{0.17}Sn(OH)_6$ perovskite hydroxides require an overpotential of 1.48 eV to adsorb OOH* intermediates following Fe^{3+} substitution, which is lower than the Co site in $CoSn(OH)_6$ (1.77 eV). The Fe^{3+} dopants thus can reduce the rate-limiting step's reaction energy barrier and provide a comparatively simple reaction path for OER.[24, 38] Therefore, DFT theoretical calculation show that appropriate Fe^{3+} doping can slightly improve the d-band center of $CoSn(OH)_6$ perovskite hydroxide, which will promote the adsorption ability and reduce the OER reaction energy barrier.

3.5 Solar-driven water splitting

Direct electrolysis of water into hydrogen through the injection of renewable solar energy is the ideal method for producing sustainable energy.[56] In the following study, we built a solar-driven water splitting reaction system by utilizing $CoSn(OH)_6$-Fe1.8% nanocubes as electrocatalyst for OER (Fig. 6a). A commercial solar cell was coupled to the two-electrode system and the gas yield during the photovoltaic-electrocatalytic water splitting process was recorded using an online gas chromatograph (Fig. S13 displays the energy conversion system photograph). The light from a Xe lamp was used to simulate the sunlight. Fig. S14 displayed the Xe lamp's irradiative spectrum. The input solar energy was calculated from the value of light intensity measured by a spectroradiometer (0.309 W cm^{-2}). The actual gas yield is comparable with the theoretical gas yielding (Fig. S15). As Fig. 6b illustrates, the real gas yields of O_2 are approximate half as that of H_2. Furthermore, the Faradaic efficiency of evolved H_2 can reach as 98.21% (Fig. 6c), and it still maintained 87.17% after 160 min (Fig. S16). Furthermore, about 8.87% was calculated for solar-to-hydrogen energy conversion efficiency (Fig. 6c). The above results show that $CoSn(OH)_6$-Fe1.8% nanocubes are promising for photovoltaic-electrocatalytic water decomposition.

4. Conclusions

In summary, $CoSn(OH)_6$ perovskite hydroxides with tuned d band states by doping varying atomic ratios of Fe^{3+} were achieved. The XRD, EDX, and XPS confirmed the successful doping of Fe^{3+} into $CoSn(OH)_6$ perovskite hydroxide. The optimal Fe^{3+} content was found to be 1.8 mol% ($CoSn(OH)_6$-Fe1.8%), which showed the highest OER activity with overpotential of 289 mV at 10 mA cm^{-2} in alkaline electrolyte. In-situ Raman spectroscopy showed that there is no obvious re-construction occurred during the OER for both $CoSn(OH)_6$ and $CoSn(OH)_6$-Fe1.8%. The DFT-based density of states (DOS) analysis indicated an increase in the d-band center with after Fe^{3+} doping. The DFT calculations suggested that an appropriate incorporation of Fe^{3+} into $CoSn(OH)_6$ significantly lowers the Gibbs free energy in the rate-determining step compared to

pure-phase $CoSn(OH)_6$. In order to evaluate the potentially practical application of as-prepared $CoSn(OH)_6$-Fe1.8%, a photovoltaic-electrolysis water splitting system was established and the solar-hydrogen energy conversion efficiency can achieve 8.87%. This study provides an effective strategy to modulate the d-band center of Co-based perovskite hydroxides for promoted electrocatalytic OER.

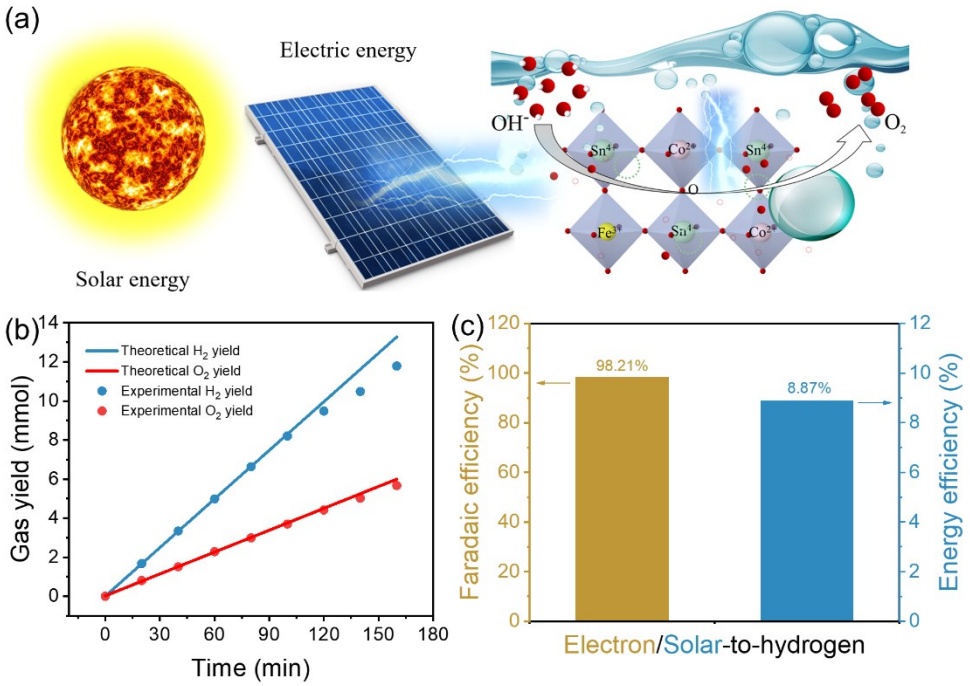

Fig. 6 (a) Schematic of solar-driven water splitting system; (b) H_2 and O_2 yields for the cathode and anode in 1 M KOH solution; (c) Faraday efficiency and the solar-to-hydrogen energy conversion efficiency at 80 min.

Author Contributions

Mingwei Sun: conceptualization, data curation, formal analysis, investigation, methodology, writing – original draft, writing – review & editing. Baopeng Yang: formal analysis. Jiaxing Yan: data curation – supporting, formal analysis – supporting. Yulong Zhou: validation – supporting. Zhencong Huang: validation – supporting. Ning Zhang: funding acquisition, project administration, resources, supervision, validation, writing – review & editing. Rong Mo: review & editing. Renzhi Ma: review & editing.

Conflicts of interest

There are no conflicts to declare.

Acknowledgements

This work received financial support from the National Natural Science Foundation of China (22072183) and the Natural Science Foundation of Hunan Province, China (2022JJ30690 and 2024JJ5378). This work was supported in part by the High Performance Computing Center of Central South University.

References

1. S. Chu and A. Majumdar, *Nature*, 2012, **488**, 294-303.
2. S. Wang, G. Liu and L. Wang, *Chemical Reviews*, 2019, **119**, 5192-5247.
3. Z. W. Seh, J. Kibsgaard, C. F. Dickens, I. Chorkendorff, J. K. Nørskov and T. F. Jaramillo, *Science*, 2017, **355**, eaad4998.
4. K. Jiao, J. Xuan, Q. Du, Z. Bao, B. Xie, B. Wang, Y. Zhao, L. Fan, H. Wang, Z. Hou, S. Huo, N. P. Brandon, Y. Yin and M. D. Guiver, *Nature*, 2021, **595**, 361-369.
5. J. Greeley, T. F. Jaramillo, J. Bonde, I. Chorkendorff and J. K. Nørskov, *Nature Materials*, 2006, **5**, 909-913.
6. S. Chu, Y. Cui and N. Liu, *Nature Materials*, 2017, **16**, 16-22.
7. N.-T. Suen, S.-F. Hung, Q. Quan, N. Zhang, Y.-J. Xu and H. M. Chen, *Chemical Society Reviews*, 2017, **46**, 337-365.
8. Y. He, L. Jia, X. Lu, C. Wang, X. Liu, G. Chen, D. Wu, Z. Wen, N. Zhang, Y. Yamauchi, T. Sasaki and R. Ma, *ACS Nano*, 2022, **16**, 4028-4040.
9. C. C. L. McCrory, S. Jung, I. M. Ferrer, S. M. Chatman, J. C. Peters and T. F. Jaramillo, *Journal of the American Chemical Society*, 2015, **137**, 4347-4357.
10. L. C. Seitz, C. F. Dickens, K. Nishio, Y. Hikita, J. Montoya, A. Doyle, C. Kirk, A. Vojvodic, H. Y. Hwang, J. K. Norskov and T. F. Jaramillo, *Science*, 2016, **353**, 1011-1014.
11. Y. Chen, H. Li, J. Wang, Y. Du, S. Xi, Y. Sun, M. Sherburne, J. W. Ager, A. C. Fisher and Z. J. Xu, *Nature Communications*, 2019, **10**, 572.
12. D. Wang and D. Astruc, *Chemical Society Reviews*, 2017, **46**, 816-854.
13. L. Wu, L. Yu, X. Xiao, F. Zhang, S. Song, S. Chen and Z. Ren, *Research*, **2020**.
14. N. Sakai, K. Fukuda, R. Ma and T. Sasaki, *Chemistry of Materials*, 2018, **30**, 1517-1523.

15. Y. Hu, F. Li, Y. Long, H. Yang, L. Gao, X. Long, H. Hu, N. Xu, J. Jin and J. Ma, *Journal of Materials Chemistry A*, 2018, **6**, 10433-10440.
16. X. Xu, F. Song and X. Hu, *Nature Communications*, 2016, **7**, 12324.
17. W. Xin, B. Liu, Y. Zhao, G. Chen, P. Chen, Y. Zhou, W. Li, Y. Xu, Y. Zhong and Y. A. Nikolaevich, *Electrochimica Acta*, 2022, **404**, 139748.
18. H. Wan, R. Ma, X. Liu, J. Pan, H. Wang, S. Liang, G. Qiu and T. Sasaki, *ACS Energy Letters*, 2018, **3**, 1254-1260.
19. S. Liu, R.-T. Gao, M. Sun, Y. Wang, T. Nakajima, X. Liu, W. Zhang and L. Wang, *Applied Catalysis B: Environmental*, 2021, **292**, 120063.
20. S.-Y. Lee, I.-S. Kim, H.-S. Cho, C.-H. Kim and Y.-K. Lee, *Applied Catalysis B: Environmental*, 2021, **284**, 119729.
21. D. Zhong, T. Li, D. Wang, L. Li, J. Wang, G. Hao, G. Liu, Q. Zhao and J. Li, *Nano Research*, 2022, **15**, 162-169.
22. S. Anantharaj, K. Karthick and S. Kundu, *Materials Today Energy*, 2017, **6**, 1-26.
23. Z. He, J. Zhang, Z. Gong, H. Lei, D. Zhou, N. Zhang, W. Mai, S. Zhao and Y. Chen, *Nature Communications*, 2022, **13**, 2191.
24. S. Liu, S. Geng, L. Li, Y. Zhang, G. Ren, B. Huang, Z. Hu, J.-F. Lee, Y.-H. Lai, Y.-H. Chu, Y. Xu, Q. Shao and X. Huang, *Nature Communications*, 2022, **13**, 1187.
25. H. Ding, H. Liu, W. Chu, C. Wu and Y. Xie, *Chemical Reviews*, 2021, **121**, 13174-13212.
26. M. A. Peña and J. L. G. Fierro, *Chemical Reviews*, 2001, **101**, 1981-2018.
27. D. Chen, M. Qiao, Y.-R. Lu, L. Hao, D. Liu, C.-L. Dong, Y. Li and S. Wang, *Angewandte Chemie International Edition*, 2018, **57**, 8691-8696.
28. Z. Wang, Z. Wang, H. Wu and X. W. Lou, *Scientific Reports*, 2013, **3**, 1391.
29. J. Suntivich, H. A. Gasteiger, N. Yabuuchi, H. Nakanishi, J. B. Goodenough and Y. Shao-Horn, *Nature Chemistry*, 2011, **3**, 546-550.
30. Z. Chen, Y. Song, J. Cai, X. Zheng, D. Han, Y. Wu, Y. Zang, S. Niu, Y. Liu, J. Zhu, X. Liu and G. Wang, *Angewandte Chemie International Edition*, 2018, **57**, 5076-5080.
31. S. Bhattacharjee, U. V. Waghmare and S.-C. Lee, *Scientific Reports*, 2016, **6**, 35916.
32. H. Zhang, F. Wan, X. Li, X. Chen, S. Xiong and B. Xi, *Advanced Functional Materials*, 2023, **33**, 2306340.
33. X. Guo, J. Shi, M. Li, J. Zhang, X. Zheng, Y. Liu, B. Xi, X. An, Z. Duan, Q. Fan, F. Gao and S. Xiong, *Angewandte Chemie International Edition*, 2023, **62**, e202314124.
34. X. Guo, J. Zhang, L. Yuan, B. Xi, F. Gao, X. Zheng, R. Pan, L. Guo, X. An, T. Fan and S. Xiong, *Advanced Energy Materials*, 2023, **13**, 2204376.
35. P. Li, S. Zhao, Y. Huang, Q. Huang, B. Xi, X. An and S. Xiong, *Advanced Energy Materials*, 2024, **14**, 2303360.
36. X. Guo, M. Duan, J. Zhang, B. Xi, M. Li, R. Yin, X. Zheng, Y. Liu, F. Cao, X. An and S. Xiong, *Advanced Functional Materials*, 2022, **32**, 2209397.
37. Z. Xiao, W. Zhou, N. Zhang, C. Liao, S. Huang, G. Chen, G. Chen, M. Liu, X. Liu and R. Ma, *Chemical Communications*, 2021, **57**, 6070-6073.
38. D. Luo, B. Yang, Z. Mei, Q. Kang, G. Chen, X. Liu and N. Zhang, *ACS Applied Materials & Interfaces*, 2022, **14**, 52857-52867.
39. S. Chen, Z. Zheng, Q. Li, H. Wan, G. Chen, N. Zhang, X. Liu and R. Ma, *Journal of Materials Chemistry A*, 2023, **11**, 1944-1953.
40. L. Kang, C. Ye, X. Zhao, X. Zhou, J. Hu, Q. Li, D. Liu, C. M. Das, J. Yang, D. Hu, J. Chen, X. Cao, Y. Zhang, M. Xu, J. Di, D. Tian, P. Song, G. Kutty, Q. Zeng, Q. Fu, Y. Deng, J. Zhou, A. Ariando, F. Miao, G. Hong, Y. Huang, S. J. Pennycook, K.-T. Yong, W. Ji, X. Renshaw Wang and Z. Liu, *Nature Communications*, 2020, **11**, 3729.
41. F. Song, K. Schenk and X. Hu, *Energy & Environmental Science*, 2016, **9**, 473-477.
42. N. S. McIntyre and M. G. Cook, *Analytical Chemistry*, 1975, **47**, 2208-2213.
43. H. Lyu, D. Yin, B. Zhu, G. Lu, Q.-Y. Liu, X. Zhang and X. Zhang, *ACS Sustainable Chemistry & Engineering*, 2020, **8**, 9404-9414.
44. S. Riyajuddin, K. Azmi, M. Pahuja, S. Kumar, T. Maruyama, C. Bera and K. Ghosh, *ACS Nano*, 2021, **15**, 5586-5599.
45. R. Sahoo, A. K. Sasmal, C. Ray, S. Dutta, A. Pal and T. Pal, *ACS Applied Materials & Interfaces*, 2016, **8**, 17987-17998.
46. L. Zhuang, L. Ge, Y. Yang, M. Li, Y. Jia, X. Yao and Z. Zhu, *Advanced Materials*, 2017, **29**, 1606793.
47. X. Jiang, W. Xu, R. Tan, W. Song and J. Chen, *Materials Letters*, 2013, **102-103**, 39-42.
48. M. Liu, K.-A. Min, B. Han and L. Y. S. Lee, *Advanced Energy Materials*, 2021, **11**, 2101281.
49. J.-Z. Zhang, Z. Zhang, H.-B. Zhang, Y. Mei, F. Zhang, P.-X. Hou, C. Liu, H.-M. Cheng and J.-C. Li, *Nano Letters*, 2023, **23**, 8331-8338.
50. W. H. Lee, M. H. Han, Y.-J. Ko, B. K. Min, K. H. Chae and H.-S. Oh, *Nature Communications*, 2022, **13**, 605.
51. X. Xing, C. Wu, G. Yang, T. Tong, Y. Wang, D. Wang, F. C. Robles Hernandez, Z. Ren, Z. Wang and J. Bao, *Materials Today Chemistry*, 2022, **26**, 101110.
52. S. She, Y. Zhu, H. A. Tahini, X. Wu, D. Guan, Y. Chen, J. Dai, Y. Chen, W. Tang, S. C. Smith, H. Wang, W. Zhou and Z. Shao, *Small*, 2020, **16**, 2006800.
53. W. Wu, S. Shi, Z. Zhang, X. Guo, L. Sun, R. Wei, J. Zhang, L. Gao, X. Pan and G. Xiao, *Journal of Colloid and Interface Science*, 2022, **619**, 407-418.
54. J. Liu, H. Liu, H. Chen, X. Du, B. Zhang, Z. Hong, S. Sun and W. Wang, *Advanced Science*, 2020, **7**, 1901614.
55. N. Zhang, B. Yang, Y. He, Y. He, X. Liu, M. Liu, G. Song, G. Chen, A. Pan, S. Liang, R. Ma, S. Venkatesh and V. A. L. Roy, *Small*, 2018, **14**, 1803015.
56. T. Faunce, S. Styring, M. R. Wasielewski, G. W. Brudvig, A. W. Rutherford, J. Messinger, A. F. Lee, C. L. Hill, H. deGroot, M. Fontecave, D. R. MacFarlane, B. Hankamer, D. G. Nocera, D. M. Tiede, H. Dau, W. Hillier, L. Wang and R. Amal, *Energy & Environmental Science*, 2013, **6**, 1074-1076.